J. Fluid Mech. (2014), *vol.* 742, *pp* 552–576. © Cambridge University Press 2014
doi:10.1017/jfm.2014.9

On the origin of the flip–flop instability of two side-by-side cylinder wakes

M. Carini[1], F. Giannetti[2] and F. Auteri[1,†]

[1]Dipartimento di Scienze e Tecnologie Aerospaziali, Politecnico di Milano, via La Masa 34, 20156 Milano, Italy

[2]Dipartimento di Ingegneria Industriale, Università degli studi di Salerno, via Ponte don Melillo, 84084 Fisciano (SA), Italy

(Received 5 March 2013; revised 1 September 2013; accepted 1 January 2014; first published online 21 February 2014)

In this work the *flip–flop* instability occurring in the flow past two side-by-side circular cylinders is numerically investigated within the range of non-dimensional gap spacing $0.6 < g < 1.4$ and Reynolds number $50 < Re \leqslant 90$. The inherent two-dimensional flow pattern is characterized by an asymmetric unsteady wake (with respect to the horizontal axis of symmetry) with the gap flow being deflected alternatively toward one of the cylinders. Such behaviour has been ascribed by other authors to a bistability of the flow, and therefore termed flip–flop. In contrast, the simulations performed herein provide new evidence that at low Reynolds numbers the flip–flopping state develops through an instability of the in-phase synchronized vortex shedding between the two cylinder wakes. This new scenario is confirmed and explained by means of a linear global stability investigation of the in-phase periodic base flow. The Floquet analysis reveals indeed that a pair of complex-conjugate multipliers becomes unstable having the same low frequency as the gap flow flip-over. The neutral curve of this secondary instability is tracked within the above range of gap spacing. The spatiotemporal shape of the unstable Floquet mode is then analysed and its structural sensitivity is considered in order to identify the 'core' region of the flip–flop instability mechanism.

Key words: instability, wakes/jets, vortex streets

1. Introduction

The incompressible flow past two side-by-side circular cylinders represents one of the prototypical flow configurations that has been widely used to investigate interference phenomena in bluff-body wakes (Zdravkovich 1977). For such configuration it is well known that different flow regimes can occur depending on the value of the non-dimensional gap spacing between the two cylinder surfaces $g = g^*/D$ (see figure 2) and the Reynolds number $Re = U^*_\infty D^*/\nu$, where U^*_∞ denotes the free-stream velocity, D^* the cylinder diameter and ν the kinematic viscosity, see Sumner (2010) for a recent review. When $g \gtrsim 5$, the flow interference between the

† Email address for correspondence: franco.auteri@polimi.it

wakes becomes negligible while for 1–1.2 $\lesssim g \lesssim 5$ simultaneous vortex shedding takes place either in phase or phase opposition. In addition to these synchronized patterns, asymmetric flow states have also been observed within the intermediate range $0.2 \lesssim g \lesssim 1.2$. These states are characterized by a deflected gap flow with the formation of a narrow and a wide wake. More precisely, a narrower wake is formed behind the cylinder toward which the gap flow is deflected. The narrow wake is associated with a higher drag coefficient and a higher vortex-shedding frequency than those associated with the wider wake. In some cases the gap flow is found to switch randomly between the two opposite directions describing the so-called *flip–flopping* behaviour.

The switchover of the gap flow deflection has been observed both in experiments (Bearman & Wadcock 1973; Kim & Durbin 1988; Sumner *et al.* 1999; Zhou, Zhang & Yiu 2002) and numerical simulations (Chen, Tu & Yeoh 2003; Kang 2003; Afgan *et al.* 2011). In their experimental investigations at $g = 0.75$ and $Re = 2\text{–}7 \times 10^3$, Kim & Durbin (1988) found that the time scale of the flip–flop is several orders of magnitude greater than that of vortex shedding and a sharp transition between the two asymmetric states has been documented by means of the base pressure signals. Still within the turbulent regime, similar features of the flip–flopping behaviour have been reported in the experimental work of Zhou *et al.* (2002) ($g = 0.5$, $Re = 5800$) and by Afgan *et al.* (2011) ($0.25 < g < 0.75$, $Re = 3000$) who performed large eddy simulations of the two-cylinder flow. In particular, a detailed analysis of the switching process was presented by Afgan *et al.* (2011), showing that, during the flip-over, an approximately in-phase vortex shedding occurs behind the two cylinders.

At low Reynolds numbers, the asymmetrical regime has been experimentally investigated by Williamson (1985) using flow visualizations: two different harmonic modes were identified for $Re < 200$ and $g < 1$ and the related vortex dynamics accurately described. In the first harmonic mode, also termed the *fundamental mode*, inner vortices that form on the gap side of the two cylinders are squeezed and amalgamated into the stronger vortices shed from the outer shear layers and a single von Kármán street is soon formed downstream. This is depicted in the sketch reported in figure 1 with the configuration of the narrow and wide wakes corresponding to an upward gap flow deflection. In the second harmonic mode the near-wake is characterized by a double vortex street on one cylinder side and a single vortex street on the outer side of the other cylinder, toward which the gap flow is deflected. In analogy with the fundamental mode, gap vortices are distorted and entrained into the thin wake.

The same vortex dynamics that characterizes the fundamental mode, along with the gap flow flip-over, has been observed experimentally by Wang, Zhou & Li (2002) at $g = 0.7$ for $150 \leqslant Re \leqslant 750$. In this work the changeover of the gap flow direction is thoroughly described by tracking the gap vortices through a sequence of flow snapshots. In particular, the authors show that the changeover phenomenon is associated with the occurrence of unusually large gap vortices. Conversely, in his work, Williamson (1985) indicates that the vortex-merging process occurs predominantly on one side of the outer wake without explicitly mentioning any flip–flopping behaviour. Based on the available information, the origin of this possible discrepancy is not clear: it could be due for instance to a slight asymmetry in the experimental apparatus.

The occurrence of the flip–flopping regime has also been investigated by Kang (2003) exploiting two-dimensional direct numerical simulations (DNS) of the flow. A complex asymmetric pattern was found to occur for $0.4 \lesssim g \lesssim 1.5$ and $50 < Re \leqslant 160$: both cylinders are characterized by alternate and irregular slow variations of the drag

coefficient that have been related by Kang (2003) to the alternate deflection of the gap flow. Differently from what has been reported for high Re, a smoother flip-over transition with a characteristic time scale only one order of magnitude greater than that of vortex shedding has been observed by this author.

The flip–flopping regime has been often interpreted as a bistable condition between two dual asymmetric flow states. In their work, Peschard & Le Gal (1996) have proposed a system of two coupled Landau oscillators to model the dynamics of the considered flow. In particular, among the other regimes, the model was able to reproduce a bistable locked state thus establishing a clear analogy to the flip–flopping behaviour. More recently the bistability conjecture has been further supported by Mizushima & Ino (2008) who performed a linear global stability analysis of the steady symmetric base flow at very low Reynolds numbers. In their work, in addition to the in-phase and antiphase harmonic modes documented by Akinaga & Mizushima (2005), a steady antisymmetric mode was described. More precisely, this mode was found responsible for the steady deflection of the gap flow owing to a pitchfork bifurcation occurring at $Re \sim 55$ and within a very narrow range of gap spacing, i.e. $0.594 \leqslant g \leqslant 0.607$. Based on these results, the two authors conjectured that the gap flow switchover may be interpreted as a transition between two dual asymmetric oscillatory flow states originating as secondary instabilities on the corresponding steady deflected flow. The authors affirm that 'Both the oscillatory states are also stable so that there exists a barrier between the two states. However, the barrier is easily overcome due to fluctuations which always exist in the flow field'. Accordingly, a stochastic framework can be used to characterize the flip–flop, similarly to what has been done by Kim & Durbin (1988) who showed that at high Reynolds numbers the time interval between two subsequent flip-overs follows a Poisson distribution.

Despite several investigations of the flip–flopping regime, a clear understanding of its origin is still lacking, thus motivating the present work. We first investigate the flip–flop instability by means of two-dimensional DNS of the flow for $g = 0.7$ and $Re \leqslant 90$. The selected value of the gap width is indeed consistent with the occurrence of the flip–flopping behaviour documented in the previously cited experimental and numerical works. Starting from the unstable symmetrical base flow, the herein performed DNS analysis indicates that the flip–flop develops as a secondary instability of the two cylinder wakes from the in-phase synchronized vortex shedding. This motivates a two-dimensional Floquet stability analysis of the in-phase limit cycle aimed to confirm and explain the new transition scenario. Starting from the results at $g = 0.7$, the stability analysis is then extended to an interval of gap spacing $0.6 < g < 1.4$, tracking the neutral curve associated with the unstable Floquet mode. In order to investigate the region of the flow which is responsible for the onset of the flip–flop instability, a structural sensitivity analysis of the unstable Floquet mode is also performed following the approach recently introduced by Giannetti, Camarri & Luchini (2010).

The work is organized as follows. The flow configuration and the governing equations are introduced in § 2 where the structural sensitivity theoretical background is also shortly recalled. The employed numerical procedures are summarized in § 3. DNS results are presented in § 4: both the transient evolution to the flip–flopping state and its fully developed vortex dynamics are described. Then the stability results are introduced in § 5. In particular, § 5.1 is devoted to the base flow analysis while in § 5.2 the curve of neutral stability is tracked in the parameter plane. Direct and adjoint eigenfunctions are illustrated in § 5.3, while the related structural sensitivity is examined in § 5.4. Finally, some conclusions are drawn in § 6.

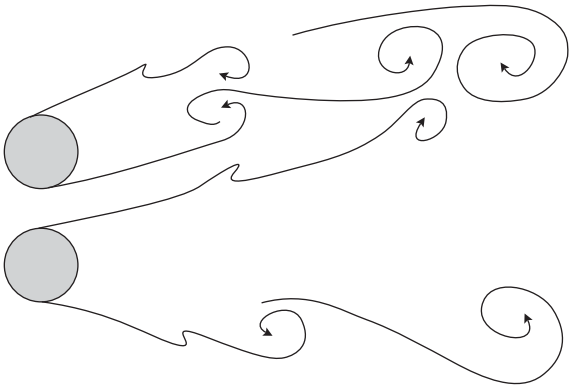

FIGURE 1. Sketch of the biased gap flow pattern and related vortex dynamics characterizing the near wake of two side-by-side cylinders during the flip–flopping regime.

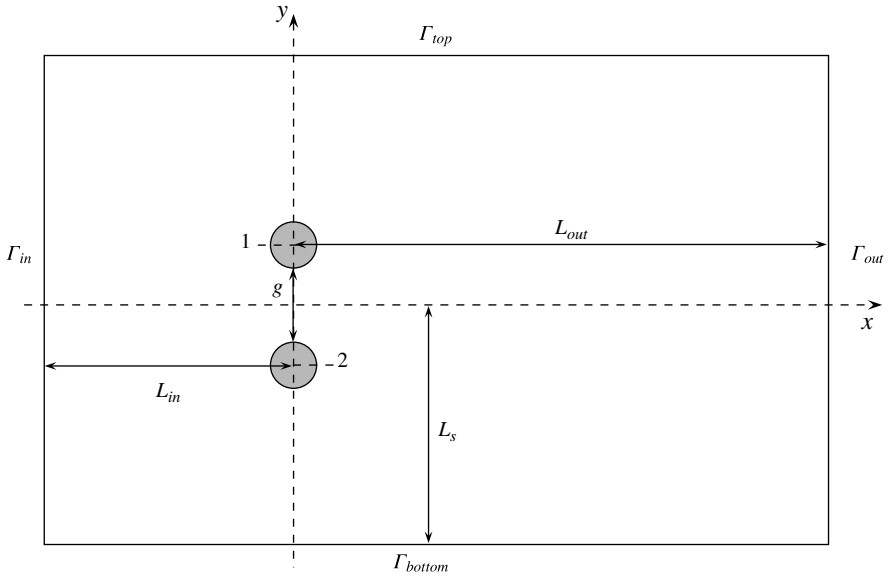

FIGURE 2. Sketch of the computational domain Ω_c employed for numerical investigations of the flow past the two circular cylinders in a side-by-side arrangement.

2. Mathematical formulation

The two-dimensional flow past two side-by-side circular cylinders of equal diameter is described using a Cartesian coordinate system which is illustrated in figure 2. The two cylinder centres are aligned on the y-axis and symmetrically placed with respect to the x-axis which is oriented as the free stream. As already mentioned, this flow configuration is completely described by two parameters: the Reynolds number Re and the non-dimensional gap spacing between the two cylinder surfaces g. The fluid motion, in the unbounded domain Ω, is governed by the unsteady incompressible

Navier–Stokes equations which are made dimensionless using the cylinder diameter D^*, the velocity of the incoming stream U^*_∞ and the constant density ρ^*:

$$\left.\begin{aligned} &\frac{\partial \boldsymbol{U}}{\partial t} + (\boldsymbol{U}\cdot\boldsymbol{\nabla})\boldsymbol{U} = -\boldsymbol{\nabla}P + \frac{1}{Re}\nabla^2\boldsymbol{U}, \\ &\boldsymbol{\nabla}\cdot\boldsymbol{U} = 0, \end{aligned}\right\} \tag{2.1}$$

where $\boldsymbol{U}$ denotes the velocity vector with components $\boldsymbol{U} = (U, V)$ and P is the reduced pressure. The above set of equations is supplemented by no-slip conditions on solid boundaries while in the far-field the flow is assumed to asymptotically approach the incoming uniform stream.

2.1. *Floquet analysis*

In the present investigation we are interested in the linear stability analysis of the in-phase synchronized vortex shedding of the two cylinder wakes with respect to two-dimensional disturbances. Following the classical approach of Floquet theory (Coddington & Levinson 1955; Drazin 2002; Bittanti & Colaneri 2009), the total flow field $\boldsymbol{Q} = \{\boldsymbol{U}, P\}$ is decomposed into the sum of a time-periodic base flow $\boldsymbol{Q}_b = \{\boldsymbol{U}_b, P_b\}$ of period T (corresponding to the in-phase shedding cycle which is a solution of equations (2.1)) and a small unsteady perturbation:

$$\left.\begin{aligned} &\boldsymbol{U}(x, y, t) = \boldsymbol{U}_b(x, y, t) + \epsilon\boldsymbol{u}(x, y, t), \\ &P(x, y, t) = P_b(x, y, t) + \epsilon p(x, y, t), \end{aligned}\right\} \tag{2.2}$$

$\epsilon \ll 1$ being the disturbance amplitude, and $\boldsymbol{u}$ and p being the velocity and pressure disturbances, respectively. Within the Floquet stability analysis framework, the linearized flow field $\boldsymbol{q} = \{\boldsymbol{u}, p\}$ is further assumed to have the following form:

$$\boldsymbol{q}(x, y, t) = \hat{\boldsymbol{q}}(x, y, t)\exp(\sigma t), \tag{2.3}$$

where $\sigma \in \mathbb{C}$ is the Floquet exponent while $\hat{\boldsymbol{q}} = \{\hat{\boldsymbol{u}}, \hat{p}\}$ denotes a non-trivial, periodic, complex-valued field having the same period T as the base flow. By introducing (2.2) in (2.1) with the ansatz (2.3) and after dropping nonlinear terms in ϵ, it easy to verify that $\hat{\boldsymbol{q}}$ satisfies the following form of the linearized Navier–Stokes equations (LNSEs):

$$\left.\begin{aligned} &\frac{\partial \hat{\boldsymbol{u}}}{\partial t} + \sigma\hat{\boldsymbol{u}} + \mathscr{L}\{\boldsymbol{U}_b, Re\}\hat{\boldsymbol{u}} + \boldsymbol{\nabla}\hat{p} = \boldsymbol{0}, \\ &\boldsymbol{\nabla}\cdot\hat{\boldsymbol{u}} = 0, \end{aligned}\right\} \tag{2.4}$$

where $\mathscr{L}\{\boldsymbol{U}_b, Re\}$ stands for the 'linearized Navier–Stokes operator':

$$\mathscr{L}\{\boldsymbol{U}_b, Re\}\hat{\boldsymbol{u}} = (\boldsymbol{U}_b\cdot\boldsymbol{\nabla})\hat{\boldsymbol{u}} + (\hat{\boldsymbol{u}}\cdot\boldsymbol{\nabla})\boldsymbol{U}_b - \frac{1}{Re}\nabla^2\hat{\boldsymbol{u}}. \tag{2.5}$$

The above equations are completed by homogeneous boundary conditions on the solid walls, by appropriate far-field radiation conditions (see Giannetti & Luchini 2007) and by the time-periodicity constraint for $\hat{\boldsymbol{q}}$. An eigenvalue problem is thus obtained: the flow is linearly unstable at a given Reynolds number if at least a non-trivial solution of (2.4) exists such that the norm of the associated Floquet multiplier $\mu = \exp(\sigma T)$ is greater than 1 or, equivalently, if the real part of the associated Floquet exponent $\lambda = \mathrm{Re}(\sigma) > 0$.

2.2. *Adjoint equations and structural sensitivity*

In addition to the Floquet modes $\hat{\boldsymbol{q}}(x, y, t)$, in this paper we will make use of properties of the solution of the adjoint eigenvalue problem. In particular it is assumed that the form of the flow field adjoint to $\boldsymbol{q}(x, y, t)$ is $\boldsymbol{g}^{+}(x, y, t) = \hat{\boldsymbol{g}}^{+}(x, y, t)\exp(-\sigma t)$, where $\hat{\boldsymbol{g}}^{+} = \{\hat{\boldsymbol{f}}^{+}, \hat{m}^{+}\}$ is periodic in time with the same period T as the base flow. The adjoint modes therefore satisfy the following set of equations

$$\left.\begin{array}{l} \dfrac{\partial \hat{\boldsymbol{f}}^{+}}{\partial t} - \sigma\,\hat{\boldsymbol{f}}^{+} + \mathscr{L}^{+}\{\boldsymbol{U}_b, Re\}\hat{\boldsymbol{f}}^{+} + \boldsymbol{\nabla}\hat{m}^{+} = \boldsymbol{0}, \\ \boldsymbol{\nabla}\cdot\hat{\boldsymbol{f}}^{+} = 0, \end{array}\right\} \tag{2.6}$$

with homogeneous boundary conditions on the cylinder surfaces, appropriate radiation conditions in the far field and the periodicity constraint for $\hat{\boldsymbol{g}}^{+}$ in time. We refer to Giannetti *et al.* (2010) and Luchini, Pralits & Giannetti (2007) for the derivation of (2.6) and a discussion on the appropriate far-field conditions. The adjoint Floquet mode can be employed to study the receptivity of the direct Floquet mode to external forcing or to initial conditions (see Chomaz 2005 and Giannetti & Luchini 2007). In order to identify the regions of the flow where the instability mechanism develops, we resort here to the same approach employed by Giannetti *et al.* (2010) and Camarri & Giannetti (2010) to study the secondary instability of the isolated cylinder wake. This method provides indeed a generalization to periodic base flows of the 'wavemaker' concept introduced by Giannetti & Luchini (2007) within a global framework and successively used in many studies to better understand the nature of the global instabilities arising in different geometries and settings and to develop appropriate passive and active strategies to control them (see, among others, Marquet, Sipp & Jacquin (2008), Giannetti, Luchini & Marino (2009), Marino & Luchini (2009), Camarri & Iollo (2010), Meliga, Sipp & Chomaz (2010), Pralits, Brandt & Giannetti (2010), and Ilak *et al.* (2011) for cases involving Newtonian fluids and Lashgari *et al.* (2012) and Haque *et al.* (2012) for examples involving non-Newtonian fluids). In particular, using a similar procedure, a structural perturbation of the Floquet eigenproblem is carried out with the aim of determining the region of the flow having the role of 'wavemaker' in the excitation of the considered global instability. For such purpose a localized structural perturbation of the linearized momentum equation in (2.4) is considered. Indicating with LHS the left-hand side of the first equation of (2.4), such perturbation is assumed to have the following form:

$$\mathrm{LHS} = \delta(x - x_0, y - y_0)C_0 \cdot \hat{\boldsymbol{u}}, \tag{2.7}$$

where C_0 is a generic constant (feedback) matrix, the symbol '$\cdot$' stands for the matrix–vector product, (x_0, y_0) are the coordinates of the point where the feedback acts and $\delta(x, y)$ denotes the Dirac delta function. This form of the structural perturbation is indeed appropriate to locate the region of the flow which is more sensitive to a feedback from the velocity field and therefore where the instability mechanism is active, i.e. 'the core of the instability' (Giannetti *et al.* 2010). It is important to note that such analysis is not sufficient *per se* to explain the physical process underlying the flow instability. Nevertheless it provides useful information to understand it. In order to develop effective control strategies using passive devices such as for instance the splitter plate studied by Kim & Durbin (1988), the structural sensitivity to modifications of the periodic base flow could be examined as well (Marquet *et al.*

2008). However, the control of the flip–flopping gap flow is beyond the scope of the present investigation and therefore the structural sensitivity to base flow modifications has not been considered here.

By carrying out a perturbation analysis of the variation of the eigenvalue σ caused by the structural perturbation (2.7), using the properties of the adjoint velocity field $\hat{\boldsymbol{f}}^+$, we obtain that $\delta\sigma = C_0 : \boldsymbol{S}(x_0, y_0)$ where the symbol ' : ' stands for double contraction of the indices and $\boldsymbol{S}$ is the sensitivity tensor of the Floquet mode defined as

$$\boldsymbol{S}(x, y) = \frac{\displaystyle\int_t^{T+t} \hat{\boldsymbol{f}}^+(x, y, t)\hat{\boldsymbol{u}}(x, y, t)\,\mathrm{d}t}{\displaystyle\int_t^{t+T}\int_\Omega \hat{\boldsymbol{f}}^+ \cdot \hat{\boldsymbol{u}}\,\mathrm{d}\Omega\,\mathrm{d}t}. \tag{2.8}$$

In the above expression, the notation $\hat{\boldsymbol{f}}^+\hat{\boldsymbol{u}}$ indicates the dyadic product between the direct and the adjoint eigenvectors. It is worthwhile to observe that the definition of the sensitivity tensor is independent of the particular feedback process which is indeed specified through the entries of the gain matrix C_0. Thus, expression (2.8) can be used to investigate the effects of a generic force–velocity coupling which is localized in space. In addition to the inspection of the different components of the sensitivity tensor, a more concise way to extract relevant information from $\boldsymbol{S}$ is to choose a norm and build a spatial sensitivity map, plotting at each spatial point the value $\|\boldsymbol{S}(x, y)\|$. Different norms can be employed on purpose: here the spectral norm is used (i.e. the square root of the maximum eigenvalue of A^HA, A^H being defined as the conjugate transpose of the square matrix A) to study the sensitivity of the Floquet exponent to a force–velocity coupling in which the force is oriented in the worst possible direction. By examining the corresponding sensitivity map it is possible to locate flow regions that are responsible for the largest drift of the Floquet exponent and thus for the arising of the instability mechanism. In addition, in order to recover phase information, a time impulsive form of the structural perturbation can also be considered

$$\mathrm{LHS} = \delta((t \bmod T) - t_0)\delta(x - x_0, y - y_0)C_0 \cdot \hat{\boldsymbol{u}}, \tag{2.9}$$

where the time instant t_0 corresponds to the precise phase at which the structural perturbation is impulsively applied. The resulting drift of the Floquet exponent σ is then given by $\delta\sigma = \boldsymbol{I}(x_0, y_0, t_0) : C_0$ where $\boldsymbol{I}$ denotes the instantaneous sensitivity tensor defined as

$$\boldsymbol{I}(x, y, t) = \frac{\hat{\boldsymbol{f}}^+(x, y, t)\hat{\boldsymbol{u}}(x, y, t)}{\displaystyle\int_t^{t+T}\int_\Omega \hat{\boldsymbol{f}}^+ \cdot \hat{\boldsymbol{u}}\,\mathrm{d}\Omega\,\mathrm{d}t}. \tag{2.10}$$

More details on the derivation and use of the above equations can be found in Luchini, Giannetti & Pralits (2008) and Giannetti *et al.* (2010).

3. Numerical approach

The DNS of the two-dimensional Navier–Stokes equations (2.1) and the related Floquet stability analysis are carried out on the rectangular computational domain Ω_c which is illustrated in figure 2. In both cases the governing equations are spatially discretized using a standard second-order finite difference scheme on Cartesian staggered grids. An immersed boundary technique is employed to simulate

the cylinder surfaces while preserving the second-order accuracy of the spatial discretization (see Giannetti & Luchini 2007 for further details). At the outlet boundary Γ_{out} the fully nonlinear equations are supplemented with the boundary conditions $-P + 2Re^{-1}\partial U/\partial x = 0$ and $\partial V/\partial x = 0$. Both at the inlet Γ_{in} and at the side boundaries Γ_{top} and Γ_{bottom}, the vorticity is set to zero and the flow perturbation produced by the two cylinders on the uniform stream is assumed to decay to zero as the leading term in the potential flow around them. More precisely, on Γ_{in} the boundary condition $U = 1 + a/r$ is imposed, where r is the radial distance from the origin while a denotes a scalar constant whose value is automatically determined within the numerical procedure. Similarly, on Γ_{top} and Γ_{bottom} the boundary condition $V = b/r$ holds, with the constant b being again implicitly assigned. To compute the Floquet mode, the above boundary conditions are applied with homogeneous data. The resulting semi-discretized equations, both for the base flow and the stability analysis, are advanced in time by the hybrid third-order Runge–Kutta/Crank–Nicolson scheme of Rai & Moin (1991): both the diffusive terms and the pressure field are treated implicitly while the convective terms are treated explicitly. Thus, for each temporal substep a Stokes-like operator is numerically inverted using the sparse LU solver provided with the free software package UMFPACK (Davis 2004).

The computation of the adjoint Floquet mode is here performed resorting to a discrete adjoint approach. This is achieved in practice by applying the adjoint procedure to the linearized problem at the code level: in this way the proper boundary conditions for the adjoint problem are accounted for automatically. Both the direct and adjoint dominant Floquet modes are then computed making use of the ARPACK library (Lehoucq, Sorensen & Yang 1998): forward/backward time marching (over one period) of the direct/adjoint discretized equations are employed to extract the dominant eigenmodes. As expected, due to the employed discrete adjoint formulation, the obtained Floquet multipliers for the direct and adjoint problems are coincident to machine precision.

The main results presented in this work have been computed within the range of gap spacing $0.6 < g < 1.4$ and Reynolds number $50 < Re \leqslant 90$. All of the results have been calculated on a domain Ω_c of length $L_x = 125$ in the streamwise direction and $L_y = 100$ in the cross-stream direction. The inlet, the outlet and the lateral boundaries are located at a distance from to origin equal to $L_{in} = 50$, $L_{out} = 75$ and $L_s = 50$, respectively. The whole computational domain is discretized using 430×450 nodes with grid points clustered near the cylinder surfaces. More precisely, a uniform mesh with the finest grid spacing of $\Delta x = \Delta y = 0.02$ is employed within the small rectangular subdomain $[-1, 1] \times [-2.5, 2.5]$ enclosing the two cylinders. Such grid will be referred to as M_0. In addition, a finer mesh M_F with a similar structure was setup for convergence studies, consisting of 700×800 points with a minimum grid spacing of $\Delta x = \Delta y = 0.01$. For time integration, a non-dimensional step of $\Delta t = 0.03$ is employed, which is reduced to $\Delta t = 0.015$ when using the M_F grid. In order to validate the adopted spatiotemporal discretization a comparison of the computed DNS results with those reported by Kang (2003) for selected values of the governing parameters is summarized in table 1. These DNS have been performed by setting $g = 1.5$ and $Re = 100$ for which an in-phase synchronized vortex shedding of the two wakes is found: the inherent flow pattern is illustrated in figure 3. Both the aerodynamic coefficients and the Strouhal number St show good agreement with the values reported by Kang (2003): the small discrepancies affecting $\bar{C}_D$ and C'_L can be mainly ascribed to the slightly different formulation of the external boundary conditions and to the different immersed boundary technique as well as to the greater

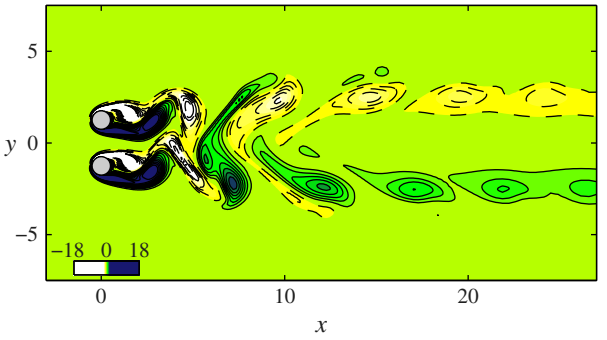

FIGURE 3. (Colour online) Flow field vorticity snapshot during in-phase synchronized vortex shedding at $g = 1.5$ and $Re = 100$.

	$\bar{C}_D$	C'_L	St
Kang (2003)	1.434	0.271	0.164
Present (M_0)	1.409	0.262	0.163
Present (M_F)	1.408	0.266	0.163

TABLE 1. Comparison of DNS results for the in-phase synchronized vortex-shedding regime at $g = 1.5$ and $Re = 100$, being $\bar{C}_D$ the mean drag coefficient, C'_L the maximum amplitude of the lift coefficient fluctuations and St the Strouhal number. Owing to vortex-shedding synchronization, all of these quantities assume the same value for both cylinders.

L_{out} size of the rectangular domain, the outlet distance employed by Kang (2003) being $L_{out} = 30$.

4. DNS results

Several numerical simulations have been performed for $g = 0.7$ while varying the Reynolds number within the considered range of values. All simulations have been initialized with the corresponding symmetric base flow which was previously computed by solving the steady version of (2.1) with standard Newton iterations. For the considered values of Re and g, the global linear stability analysis of the steady base flow has shown that two distinct unstable eigenmodes exist (Mizushima & Ino 2008). The first mode is steady and antisymmetric (AS) and it has been found responsible for the occurrence of an asymmetric steady solution which is characterized by a deflected gap flow. On the other hand, the second mode, called the *in-phase* mode (IP), is oscillatory and is responsible for the onset of the in-phase synchronized vortex shedding. Given the adopted numerical discretization and choice of the initial conditions, the primary flow instabilities are triggered only by round-off errors. Time traces of lift and drag coefficients have been used to monitor the dynamical evolution of the flow in order to shed light on the instability cascade leading to the flip–flopping behaviour. Two representative examples of such analysis are illustrated in figure 4 for $Re = 90$ and $Re = 68.8$.

At $Re = 90$, a rapid transition from the steady state to the flip–flopping regime, not shown here, occurs. During the transient, nearly periodic oscillations are established

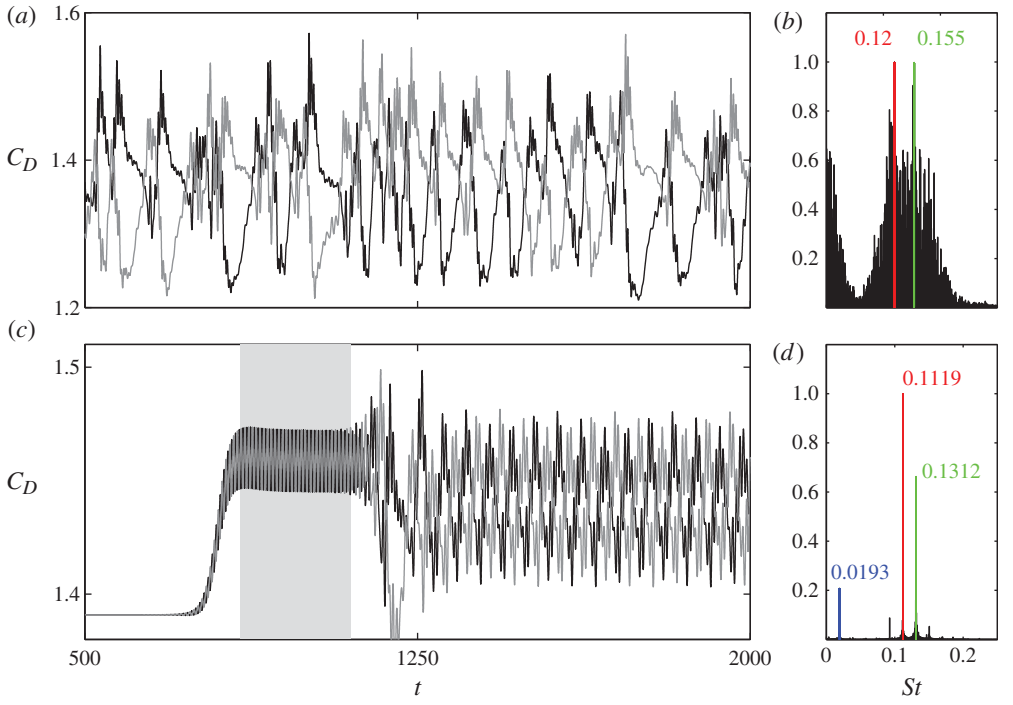

FIGURE 4. (Colour online) DNS results of the flow evolution from the steady base flow to the flip–flopping regime for $g = 0.7$ and $Re = 90$ (a,b) or $Re = 68.8$ (c,d). Parts (a,c) show the time traces of the drag coefficient: black and grey lines correspond to forces acting on cylinder 1 and 2, respectively. The grey shaded area in (c) denotes the time window associated with the appearance of the in-phase vortex-shedding cycle during the transient state. Parts (b,c) illustrate the spectral content of the lift coefficient fluctuations during the fully developed flip–flopping regime for $t \in [600, 3000]$ ($Re = 90$) (b) and $t \in [1800, 4500]$ ($Re = 68.8$) (d).

only for a few shedding cycles while periodicity is lost when the flip–flopping regime develops, showing a rather irregular behaviour of the force signals, as shown in figure 4(a). In particular, in addition to oscillations of the aerodynamic forces induced by vortex shedding, both cylinders experience alternate turns of the C_D over a time scale that is appreciably greater than that of the shedding process. The same behaviour has been described by Kang (2003) and associated to the alternate deflection of the gap flow based on the analogy with the high-Reynolds-number case. The complexity of the flip–flop dynamics at $Re = 90$ is confirmed by inspecting the spectral content of the lift fluctuations which is depicted in figure 4(b) in terms of the Strouhal number St. Despite the broadband nature of the spectra, two relevant frequency ranges can be distinguished: a low-frequency band for $St \lesssim 0.05$ and a dominant-frequency range for $0.05 \lesssim St \lesssim 0.23$ smeared around two main peaks at $St = 0.12$ and $St = 0.155$. When the Reynolds number is reduced to $Re = 68.8$ the dynamical evolution toward the flip–flop can be better understood. Starting from the steady-state solution, the flow state evolves first to a *saddle* limit cycle which corresponds to the in-phase vortex shedding and then to the flip–flopping regime. The periodic solution is established over an interval of 250 time units (≈ 29 periods) until an instability develops on the limit cycle itself leading to the flip–flop. Both

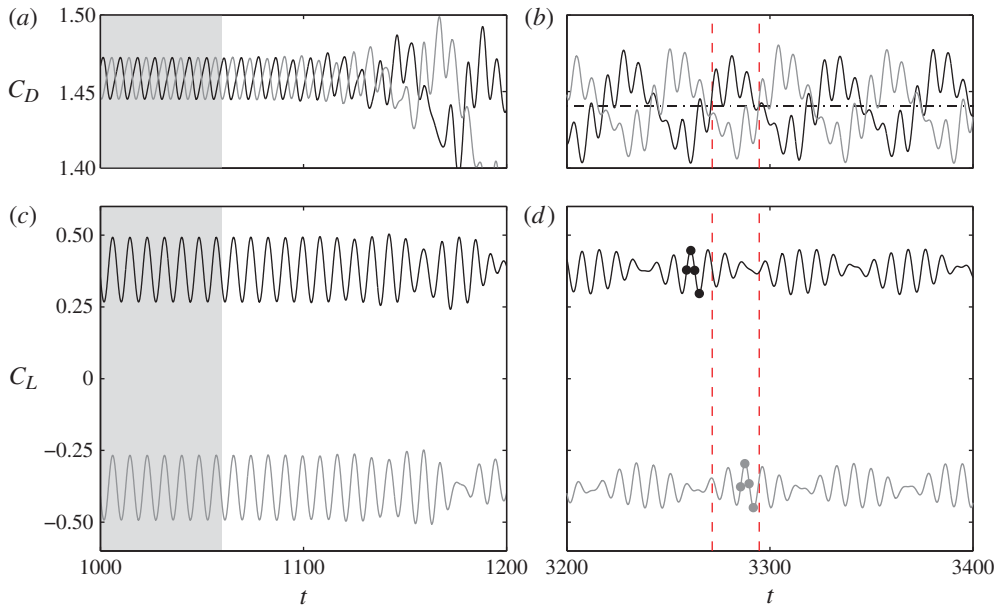

FIGURE 5. (Colour online) Details of $C_{L,1-2}$ and $C_{D,1-2}$ time traces for $g = 0.7$ and $Re = 68.8$ (see figure 4). (*a*,*c*) Development of the flip–flop instability from the in-phase vortex-shedding limit cycle. (*b*,*d*) Fully developed flip–flopping regime: round dots are used in (*d*) to mark the shedding phases associated with the vorticity snapshots reported in figure 7 while dashed vertical lines approximately indicate two subsequent gap flow flip-overs corresponding to the square dots in figure 6(*b*).

this transition and the fully developed flip–flopping state are more clearly illustrated in figure 5. The transition to the flip–flop occurs smoothly as a slow modulation of the force signals. Lift signals in figure 5(*d*) are no more in phase or in phase opposition but are generally out of phase, showing a characteristic beating-like waveform. Correspondingly, vortex-shedding-induced fluctuations of drag signals are superimposed to a slow carrier which is approximately in antiphase between the two cylinders. The relationship between the slow variations of the drag coefficients and the gap flow deflection is herein confirmed by probing the cross-stream component of the velocity field at $(x_p, y_p) = (0.5, 0)$. The sign of $V(x_p, y_p, t)$ can be assumed indeed as an indicator of the gap flow direction and its time history is illustrated in figure 6. When in-phase vortex shedding occurs ($Re = 61.6$), figure 6(*a*), gap flow oscillations are periodic and synchronized to the shedding frequency, as one would expect. Instead, during the flip–flopping regime ($Re = 68.8$), figure 6(*b*), the sign of $V(x_p, y_p, t)$ changes according to the same low-frequency oscillation which affects the drag coefficients. Thus, the gap flow remains weakly deflected toward one cylinder side for more than one shedding cycle. According to the signal of figure 6(*b*), the flip-over time instants (square dots) approximately correspond to the phase at which the drag coefficient fluctuations change sign, dashed vertical lines in figure 5(*b*).

The spectral content associated with the flip–flopping regime at $Re = 68.8$ is illustrated in figure 4(*d*). In this case the computed spectrum clearly exhibits three well-defined peaks showing a clear analogy with the results obtained at $Re = 90$. More precisely, a low-frequency peak is found at $St_1 = 0.0193$ while two dominant

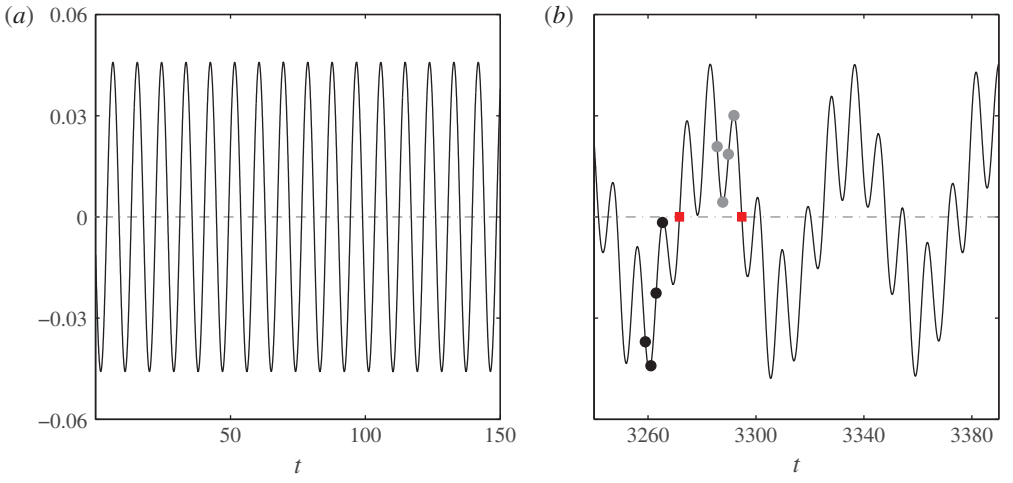

FIGURE 6. (Colour online) Time history of the cross-stream velocity component $V(x_p, y_p, t)$ at $(x_p, y_p) = (0.5, 0)$. (*a*) In-phase vortex shedding limit cycle at $Re = 61.6$ and $g = 0.7$. (*b*) Fully developed flip–flopping regime at $Re = 68.8$ and $g = 0.7$: black and grey round dots refer to vorticity snapshots in figure 7 (see also figure 5) while the two square dots approximately indicate two subsequent switching phases of the gap flow deflection.

peaks are observed at $St_2 = 0.1119$ and $St_3 = 0.1312$. The dominant harmonic at St_2 represents the in-phase vortex-shedding frequency for which $St = 0.1139$ during the periodic transient. The peak at St_1 is found to correspond to the slow oscillation of the gap flow and force coefficients. Furthermore the value of St_1 seems consistent with that of $St = 0.018$ found by Kang (2003) at $Re = 100$ and $g = 1.0$. At this point it is worthwhile to observe that the harmonic component at St_3 can be interpreted as a result of the nonlinear interaction between the former two modes, since $St_3 = St_1 + St_2$.

The flip–flopping vortex dynamics at $Re = 68.8$ is illustrated in figure 7 by means of vorticity snapshots at subsequent time instants during the vortex shedding and flip–flop processes. More precisely, the snapshots on the left- and right-hand columns of figure 7 approximately correspond to the same shedding phases but with an opposite deflection of the gap flow. This is better highlighted by the associated grey/black round markers in figure 5(*d*) and 6(*b*). The flow behind the two cylinders is clearly asymmetrical with the formation of a narrow and a wide wake according to the direction of the gap flow. Moving downstream, a single large-scale vortex street is soon formed from the outer shear layers due to the biased merging process of the inner vortices. This is well described by the sequence of figure 7(*a*,*b*,*c*,*d*) when the gap flow is deflected downwards. Indeed during one shedding cycle both counter-rotating inner vortices are weakened and amalgamated on the upper side of the wake with a mechanism which appears very similar to the vortex dynamics observed by Wang *et al.* (2002) and to the asymmetric fundamental shedding mode described by Williamson (1985) at $g = 0.85$ and $Re = 200$. Specular dynamics are observed in figure 7(*f*,*g*,*h*,*i*) where the gap flow is directed downward and the gap vortices are merged on the lower side of the large-scale vortex street. The snapshots reported in figure 7(*e*,*j*) approximately correspond to the phase where the gap flow changes its deflection, as marked in figure 6(*b*) by square dots. As reported by

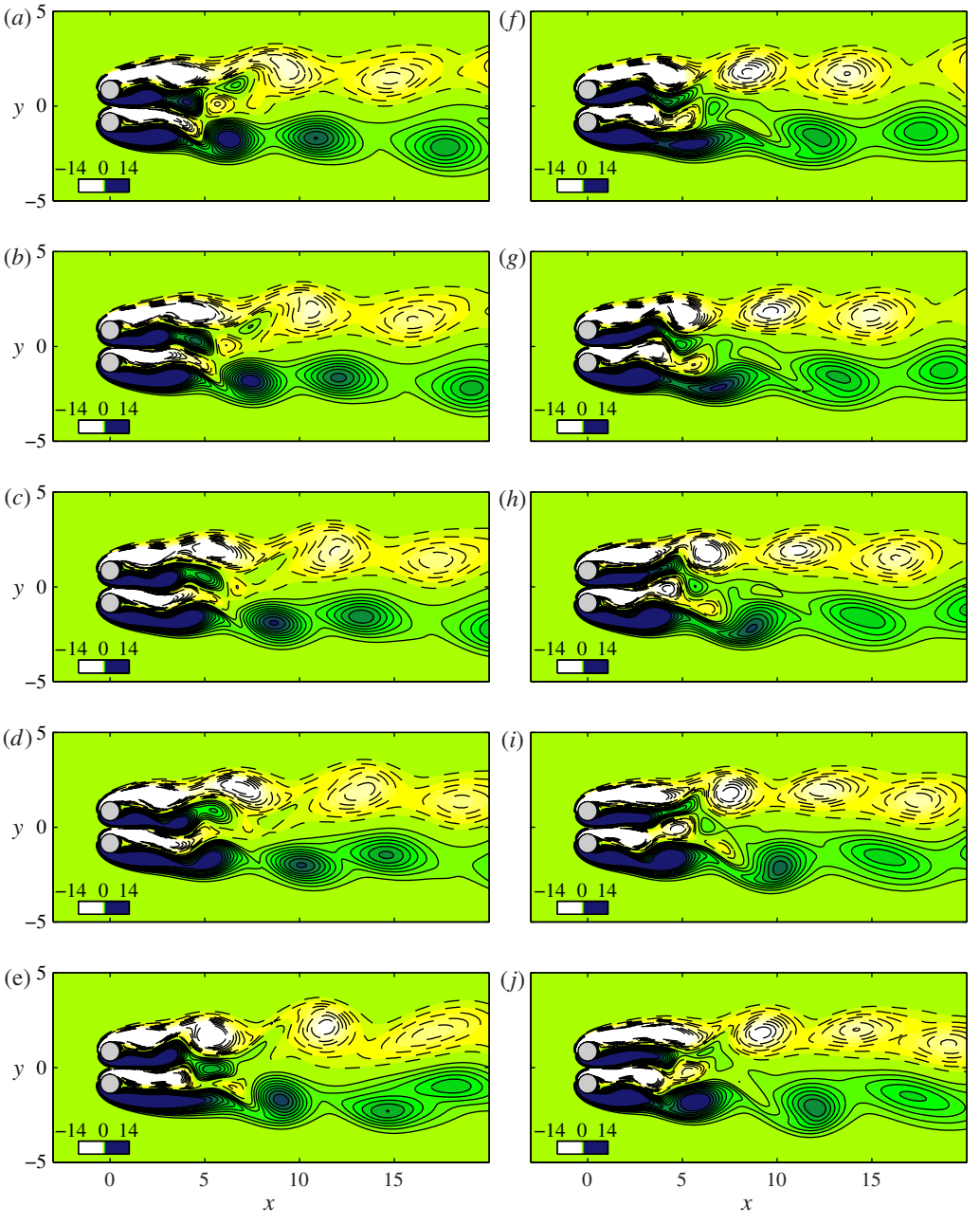

FIGURE 7. (Colour online) Flow-field vorticity snapshots of the fully developed flip–flopping regime at $g = 0.7$ and $Re = 68.8$. Black round dots are used in figure 5(*d*) and figure 6(*b*) to mark shedding phases corresponding to snapshots (*a*), (*b*), (*c*) and (*d*) for which a weakly downward deflected gap flow is observed. Similarly, snapshots (*f*), (*g*), (*h*) and (*i*) correspond to the grey dots in figure 5(*d*) and figure 6(*b*). Here the gap flow is deflected upward. Snapshots (*e*) and (*j*) correspond to the square dots in figure 6(*b*) where the gap flow deflection switches from downward to upward and vice versa, respectively.

Wang *et al.* (2002), when the switchover occurs quite large vortices detach from the gap shear layers. In addition, as can be also observed in the experimental visualizations in the same paper (figure 7), these larger gap vortices are remarkably convected up to the symmetry axis.

5. Stability and sensitivity results

The DNS results presented in § 4 suggest that at low Reynolds numbers the flip–flopping state originates through an instability of the in-phase synchronized vortex shedding. To the best of the authors knowledge this transition scenario has not been described in the past literature where, on the contrary, the flip–flop is often interpreted as the bistable interplay of two dual asymmetric states. These new results have motivated the following linear stability and sensitivity investigation of the time periodic in-phase vortex shedding within the theoretical framework introduced in § 2.

5.1. *Periodic base flow*

The in-phase synchronized vortex shedding of two side-by-side cylinder wakes has been described by several authors (Williamson 1985; Sumner *et al.* 1999; Kang 2003). At low Reynolds numbers, this flow pattern has been mainly observed in the range $1.5 \lesssim g \lesssim 5$ along with the dual antiphase pattern (Kang 2003). However, differently from this latter case, the idealized antisymmetrical double vortex street configuration is not 'stable' and a single large-scale vortex street is instead realized. The inherent vortex dynamics has been accurately described by Williamson (1985): like-signed vortices shed at the same time pair up, merge and rotate around each other leading to the formation of the so-called 'binary street'. An example of such transition is represented in figure 3 by a vorticity snapshot of the computed flow field at $Re = 100$ and $g = 1.5$. When reducing the gap width to $g = 0.7$, the resulting in-phase pattern appears still characterized by the formation of a single large-scale vortex street, but the underlying vortex dynamics is different from that described by Williamson (1985). This is illustrated in figure 8 where the in-phase shedding cycle at $Re = 61.6$ has been represented at different shedding phases ϕ. During one period each small gap vortex is entrained between two subsequent big vortices shed from the outer shear layer on the opposite cylinder side. Thus, gap vortices are merged on opposite sides of the outer large-scale street. The in-phase synchronization of the shedding process is confirmed by comparing the time traces of the two lift coefficient fluctuations $\Delta C_{L,1-2}$ which are shown in figure 9(*a*).

The T-periodic in-phase flow obeys a reflectional symmetry about the x-axis when time is advanced of $T/2$: this is clearly highlighted by selected shedding phases in figure 8. The same spatiotemporal symmetry has been found to characterize the two-dimensional wake past a single cylinder and following Robichaux, Balanchadar & Vanka (1999) this symmetry is called reflectional–translation (RT):

$$\left.\begin{aligned} U(x, y, t) &= U(x, -y, t + T/2), \\ V(x, y, t) &= -V(x, -y, t + T/2). \end{aligned}\right\} \tag{5.1}$$

In order to perform a Floquet analysis of the in-phase shedding cycle, the inherent periodic base flow has been computed for different values of Re and g based on a preliminary DNS analysis. In figure 9(*b*), for instance, the base flow Strouhal number St_b is plotted in the neighbourhood of the critical flip–flop threshold for $g = 0.7$ as a function of Re. As expected, the shedding frequency varies almost linearly and

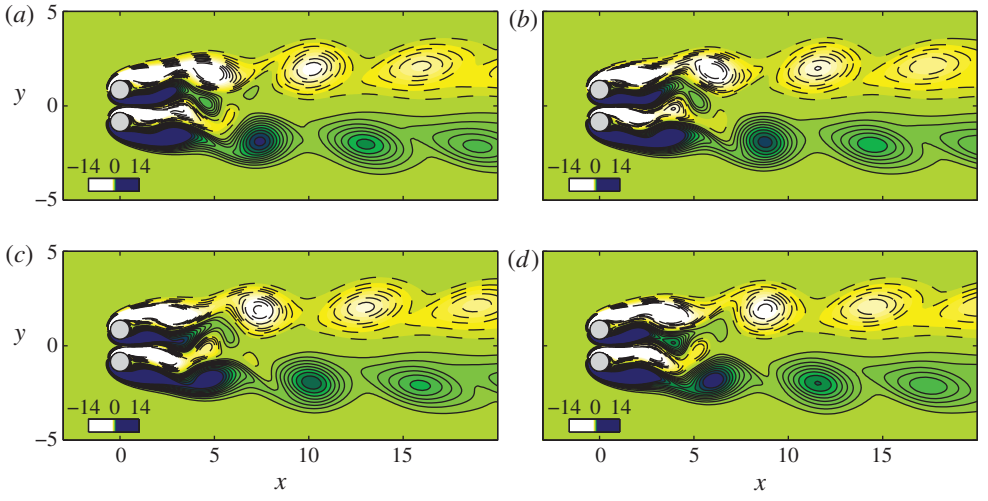

FIGURE 8. (Colour online) Vorticity snapshots of the periodic base flow for $g = 0.7$ and $Re = 61.6$. Different shedding phases ϕ among the eight in which the base flow has been equally divided are reported (see also figure 9): (*a*) $\phi = \pi/2$; (*b*) $\phi = \pi$; (*c*) $\phi = 3\pi/2$; (*d*) $\phi = 2\pi$.

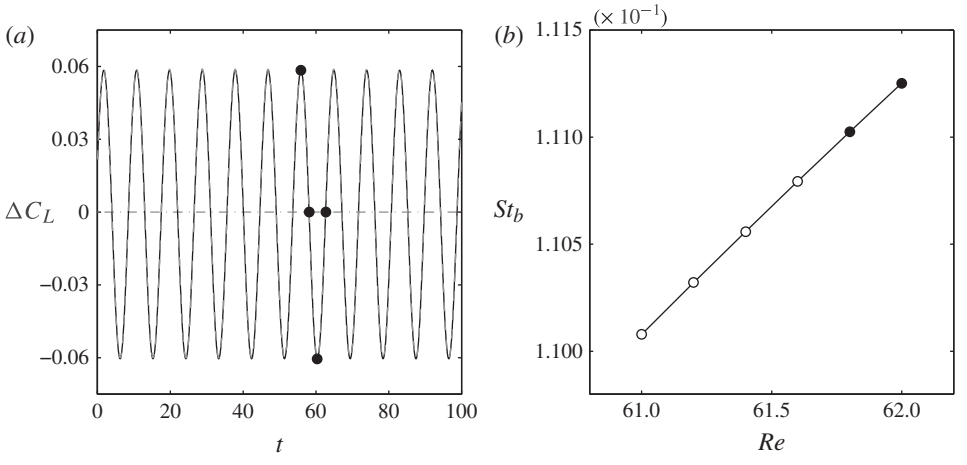

FIGURE 9. (Colour online) In-phase vortex shedding limit cycle for $g = 0.7$ and $Re = 61.6$. (*a*) Lift coefficient fluctuations $\Delta C_L = C_L(t) - \bar{C}_L$ for cylinder 1 (black lines) and cylinder 2 (grey dashed lines): black dots are employed to mark shedding phases corresponding to the vorticity snapshots in figure 8. (*b*) Strouhal number of the periodic base flow St_b at increasing Reynolds numbers in the neighbourhood of the flip–flop critical threshold: black filled dots denote the unstable periodic solutions.

compares well with the frequency St_{IP} of the unstable IP mode: for $Re = 61.8$, $St_b = 0.111$ is found while $St_{IP} = 0.1057$.

It is worthwhile to note that above the critical flip–flop threshold, the in-phase base flow cannot be simply recovered by means of standard DNS and a stabilization algorithm is needed to compute the periodic orbit. In order to stabilize the periodic

orbit, several techniques can be adopted. A quite standard approach is the one proposed by Lust *et al.* (1998) which relies on the recursive projection method (Shroff & Keller 1993). Another possibility is to use the selective frequency damping method proposed by Åkervik *et al.* (2006) (see also Viaud, Serre & Chomaz 2011), provided that the frequency of the periodic base flow is well separated from the frequency of the unstable mode, as in the present case. In this paper a different approach has been used for convenience. Basically our stabilization technique relies on a novel algorithm inspired by the iterant recombination method to accelerate fixed-point iterations by correcting the next iteration with a linear combination of the previous ones (Trottenberg, Oosterlee & Schüller 2001; P. Luchini, Private communication, 2011). This algorithm is similar to a generalized minimal residual (GMRES), but it is able to continuously update the subspace of vectors used to obtain the new estimate. The present method works in presence of both steady and unsteady bifurcations and it has been already used in conjunction with a three-dimensional multigrid solver to study the imperfect bifurcation arising in the flow over a rotating sphere (Giannetti *et al.* 2012). As an example of the effectiveness of such stabilization procedure, figure 10(*a*) illustrates the convergence history of St_b for the unstable periodic base flow computed at $Re = 62$ and $g = 0.7$, n being the number of iterations. During the iterative process, each step involves the time integration of equations (2.1) until an *ad-hoc* scalar surrogate of the periodicity condition $\boldsymbol{U}_b(t + T) = \boldsymbol{U}_b(t)$ is satisfied. Non-periodic perturbations affecting the resulting flow field are then damped by the stabilization algorithm. The trend of the residual associated with the periodicity condition $\boldsymbol{r} = \boldsymbol{U}_b(t+T) - \boldsymbol{U}_b(t)$ is shown in figure 10(*b*) by means of its infinity norm, $\|\boldsymbol{r}\|_\infty$: for the considered case 65 iterations are required to achieve $\|\boldsymbol{r}\|_\infty < 10^{-9}$.

5.2. *Neutral stability curve*

Based on the DNS results, the Floquet analysis of the in-phase shedding cycle has been started for $g = 0.7$ in the narrow range $61 \leqslant Re \leqslant 62$ with step increments of 0.2. Obtained results indicate that a single pair of complex-conjugate Floquet multipliers becomes unstable above the critical threshold of $Re \sim 61.74$. Both the growth rate $\lambda = \mathrm{Re}(\sigma)$ and the non-dimensional frequency $St_F = \mathrm{Im}(\sigma)/2\pi$ of the unstable Floquet exponent are shown in figure 11 as a function of Re. Moreover the Floquet spectrum computed for $Re = 67$ and $Re = 80$ is shown in figure 12(*a*) and (*b*), respectively. As it is evident from the figure, no other modes become unstable by increasing the Reynolds number up to $Re = 80$. The frequency St_F of the unstable Floquet mode compares well with the value St_1 detected from the DNS analysis at $Re = 68.8$ (figure 4*d*), thus confirming that the origin of the flip–flopping instability is a torus (Neimark–Sacker) bifurcation of the in-phase shedding cycle. The results obtained from the Floquet analysis for $g = 0.7$ are summarized in table 2. Starting from these results, the critical Reynolds number threshold associated with the unstable Floquet mode has been tracked as a function of the gap spacing in the range $0.6 < g < 1.4$. The resulting neutral curve is depicted in figure 13 where the neutral curve of the IP mode is also reported. Since for $g \lesssim 0.6$, other modes become unstable on the steady symmetric base flow (see figure 11 in Mizushima & Ino 2008), we restricted our analysis to $g > 0.6$. The domain of instability, highlighted by the grey shaded area in the figure, reproduces very well the parameter region where the flip–flop has been observed by Kang (2003). Also shown in figure 13 are the non-dimensional frequencies associated with both the base flow (figure 13*b*) and the unstable Floquet mode (figure 13*c*) as a function of the gap spacing moving along the neutral curve.

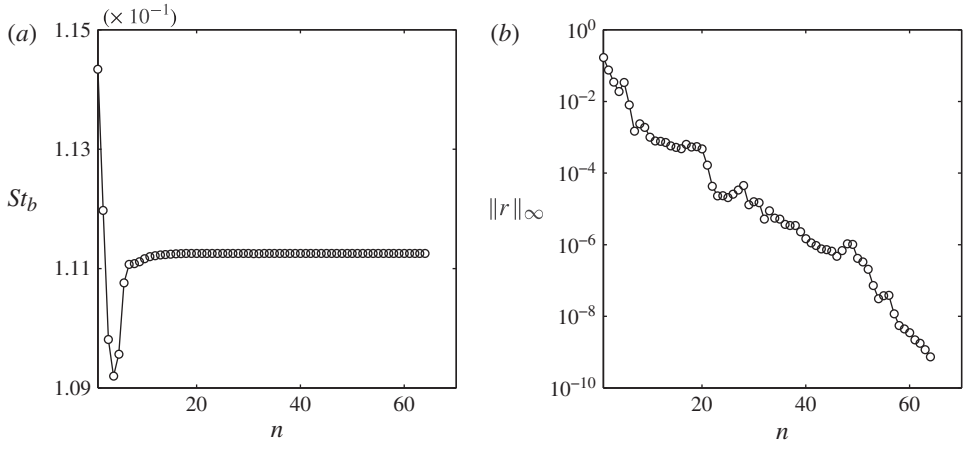

FIGURE 10. Periodic base flow stabilization for $g = 0.7$ and $Re = 62$. (a) Base flow Strouhal number $St_b = 1/T$ and (b) infinity norm of the residual on the periodicity condition $\|\boldsymbol{r}\|_\infty$, both plotted as a function of the number of iterations n.

Re	St_b	$\mathrm{Re}(\sigma) \times 10^3$	$\mathrm{Im}(\sigma)/2\pi$	$\bar{C}_D$	$\bar{C}_L$	$C'_D \times 10^2$	C'_L
61.0	0.11008	−7.3640	0.019085	1.4776	0.3932	0.8243	0.05431
61.2	0.11032	−5.2779	0.019479	1.4774	0.3929	0.8464	0.05611
61.4	0.11056	−3.2654	0.019861	1.4772	0.3926	0.8677	0.05789
61.6	0.11079	−1.3193	0.020229	1.4769	0.3923	0.8883	0.05964
61.8	0.11102	0.5689	0.020586	1.4766	0.3920	0.9082	0.06136
62.0	0.11125	2.4049	0.020932	1.4763	0.3916	0.9275	0.06306

TABLE 2. Results of the Floquet stability analysis close to the flip–flop threshold and aerodynamic coefficients of the corresponding periodic base flow for $g = 0.7$.

The non-dimensional frequency St_b scales almost linearly with g up to $g \approx 1.38$ where a steep increment is observed. The same steep increment occurs for St_F. This behaviour seems to indicate a change in the properties of the flow instability which could be related to the change in the bifurcation nature, from supercritical to subcritical, that is found to occur in the neighbourhood of $g = 1.4$ through DNS analysis. For $1.4 < g < 2.2$ a transition region between the IP mode and the flip–flop behaviour has been described by Kang (2003). However the Floquet analysis has not been extended to gap values larger than $g = 1.4$ owing to the subcritical nature of the bifurcation whose careful investigation is beyond the scope of the present work.

5.3. *Direct and adjoint Floquet mode*

The spatiotemporal structure of the unstable Floquet mode has been investigated for $g = 0.7$, a value for which the flip–flopping behaviour has been observed experimentally by Wang *et al.* (2002) at $Re = 150$. The vorticity field associated with the direct Floquet mode $\hat{\boldsymbol{u}}(x, y, t)$ is illustrated in figure 14 by means of its real component: snapshots 14(a,b,c,d) correspond to the four phases $\phi = 0, \pi/4, \pi/2, 3\pi/4$ among the eight in which the shedding cycle has been equally divided. The mode

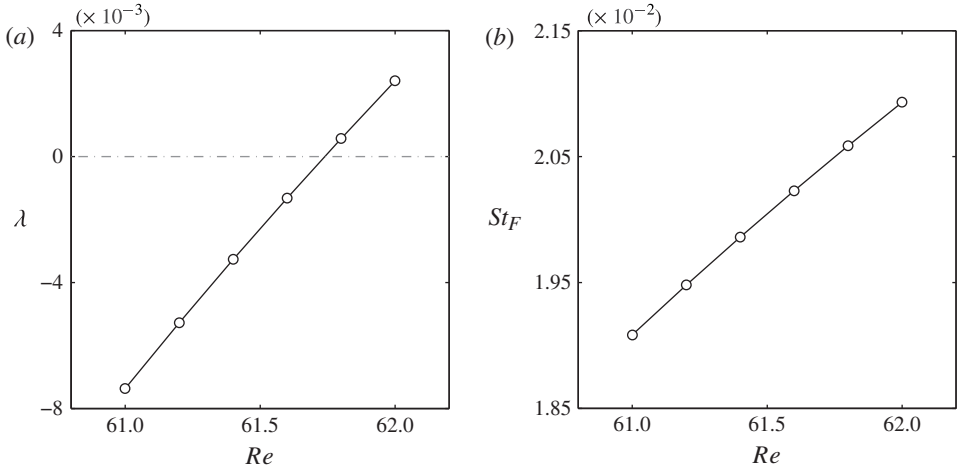

FIGURE 11. Floquet exponent σ as a function of Re in the neighbourhood of the critical threshold for $g = 0.7$. (*a*) Growth-rate $\lambda = \mathrm{Re}(\sigma)$. (*b*) Strouhal number $St_F = \mathrm{Im}(\sigma)/2\pi$.

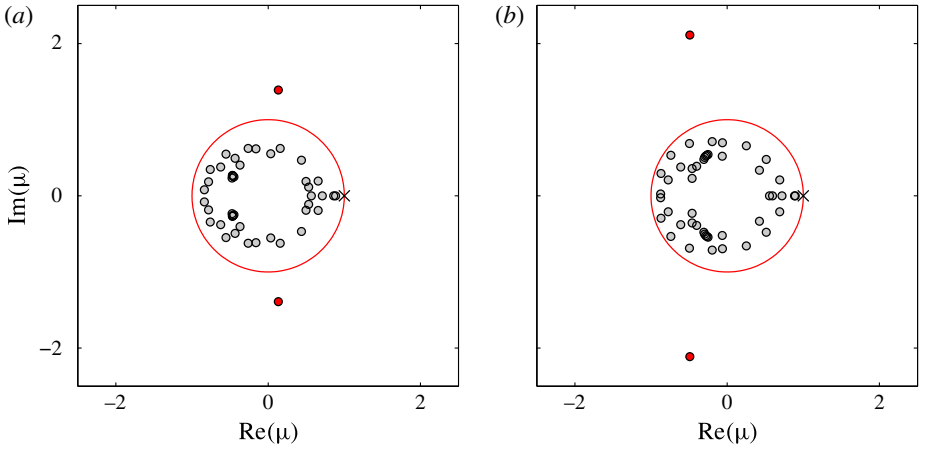

FIGURE 12. (Colour online) Floquet spectrum computed for two values of Reynolds number above the critical flip–flop threshold at $g = 0.7$: (*a*) $Re = 67$; (*b*) $Re = 80$. In each figure 50 multipliers are reported. The cross is used to denote the unitary multiplier lying on the unit circle, while the two unstable complex-conjugate multipliers lie outside the unit circle.

is characterized by the opposite spatiotemporal symmetry with respect to the base flow:

$$\left.\begin{aligned} \hat{u}(x, y, t) &= -\hat{u}(x, -y, t + T/2), \\ \hat{v}(x, y, t) &= \hat{v}(x, -y, t + T/2). \end{aligned}\right\} \tag{5.2}$$

Hence, the remaining phases can be easily recovered from those herein illustrated. Although complicated, the depicted time-periodic perturbation field shows a strong correlation with the described flip–flop dynamics. The mode structure results mainly concentrated in the near-wake region where an irregular shedding pattern is observed

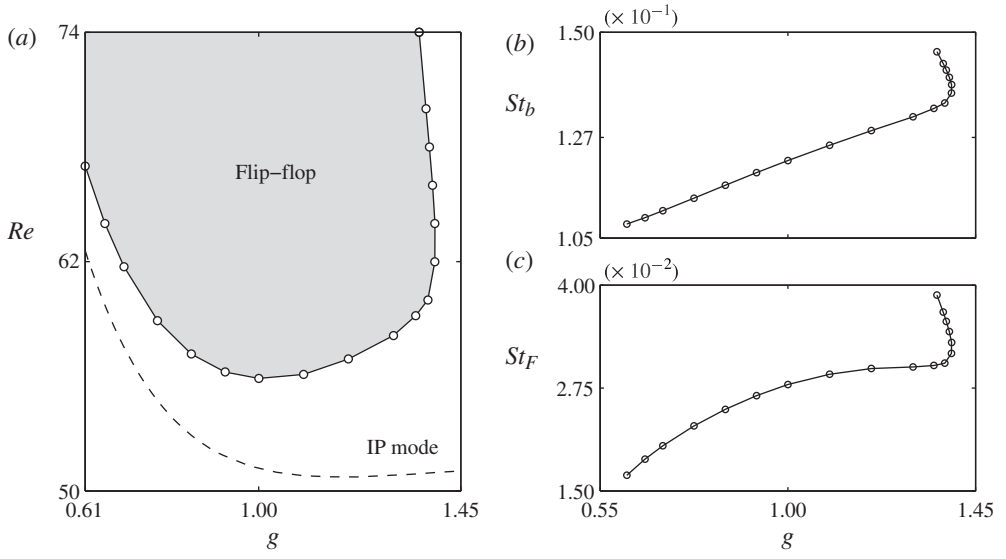

FIGURE 13. Results of the Floquet stability analysis in the parameter plane (g, Re). (a) Neutral curve associated with the unstable Floquet mode (continuous line): the grey shaded area is used to denote the region of linear instability of the periodic base flow; the dashed line corresponds to the neutral curve associated with the unstable IP mode on the steady symmetric base flow. Here St_b and St_F are plotted as a function of g moving along the neutral curve in (b) and (c), respectively.

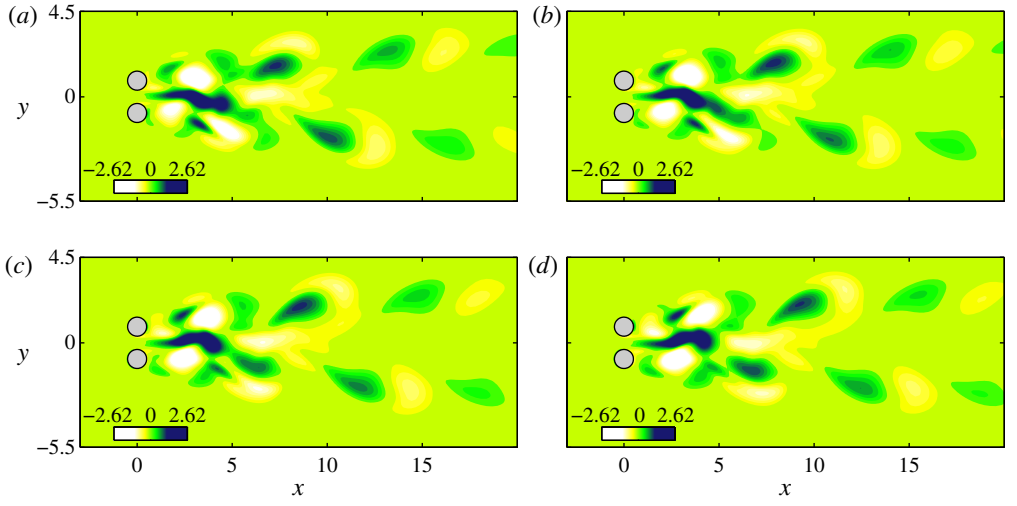

FIGURE 14. (Colour online) Vorticity field of the direct Floquet mode $\hat{\boldsymbol{u}}(x, y, t)$ (real part) evaluated at $g = 0.7$ and $Re = 61.8$. Four subsequent shedding phases ϕ are illustrated among the eight in which the vortex-shedding cycle has been equally divided: (a) $\phi = 0$; (b) $\phi = \pi/4$; (c) $\phi = \pi/2$; (d) $\phi = 3\pi/4$.

behind each cylinder. Meanwhile a strong vortical structure develops from the gap flow and between the two cylinder wakes, being related to the low-frequency deflection of the gap jet. Indeed its vorticity sign keeps constant over the period T and changes according to the superposed harmonic variation associated with the imaginary part of the Floquet exponent. Furthermore, a shedding-like mechanism takes place at the downstream edge of this region and a counter-clockwise rotating vortex is alternately shed on each cylinder side during one period T. This mechanism seems to be at the root of the biased merging process of gap eddies which characterizes the flip–flop vortex dynamics.

The magnitude of the related adjoint field is also represented in figure 15 using the same shedding phases which have been employed for the direct mode representation. Regions of maximum receptivity are located close to the outer and inner shear layers while smaller values of $\|\hat{\boldsymbol{f}}^{+}\|$ are found also within the gap flow region.

5.4. *Wavemaker investigation*

In order to provide useful information to investigate the physical nature of the flip–flopping instability, its instability core has been located by means of the structural sensitivity analysis described in § 2.2. This analysis is not sufficient to unveil the physical mechanism of instability but it gives precious information about it by localizing the region of the flow where it is active.

Figure 16(*a*) shows the sensitivity map computed using the spectral norm of $\boldsymbol{S}(x, y)$ at $Re = 61.8$ and $g = 0.7$. Different tensor norms, such as the trace or Frobenius norm could have been used as well but would not lead to significantly different results and are not reported for brevity. With reference to figure 16(*a*), it is worthwhile to note that the sensitivity tensor $\boldsymbol{S}$ vanishes almost everywhere except for a sharply localized region in the near-wake of the two cylinders. According to Giannetti & Luchini (2007) this region corresponds to the core of the instability mechanism, i.e. the so-called wavemaker. In the present case the wavemaker structure is characterized by four main peaks symmetrically placed with respect to the x-axis. More precisely the maximum sensitivity is attained within two elongated lobes in the streamwise direction which are approximately located at the edges of the expanding gap jet. This is highlighted in figure 16(*a*) where the streamlines of the mean base flow are also illustrated. Their superposition to the filled contour levels of the structural sensitivity is consistent with the meaning of (2.8) as an average sensitivity over the period T. The remaining two lower peaks are instead located on the outer sides of the two averaged wakes. It is quite surprising that the map of figure 16(*a*) shows strong analogies with the corresponding sensitivity maps of the IP and AS modes which are illustrated in figure 16(*b*) and 16(*c*), respectively. As a matter of fact, the average periodic base flow and the steady base flow have the same topological structure and similar flow regions are identified by the wavemaker analysis as the core of their respective instabilities. This is especially true for the regions of maximum sensitivity in figure 16(*a*,*c*).

In order to recover phase information about the structural sensitivity, the instantaneous sensitivity tensor (2.10) has been also computed. The spectral norm of $\boldsymbol{I}(x, y, t)$ is plotted in figure 17 at the same four shedding phases that have been used for the direct and adjoint mode in figures 14 and 15, respectively. Similarly to the time-averaged sensitivity map, the norm of $\boldsymbol{I}$ is also sharply localized having two dominant peaks located within the two vorticity layers of opposite sign developing from the cylinder surfaces in the gap region. The amplitude and position of such

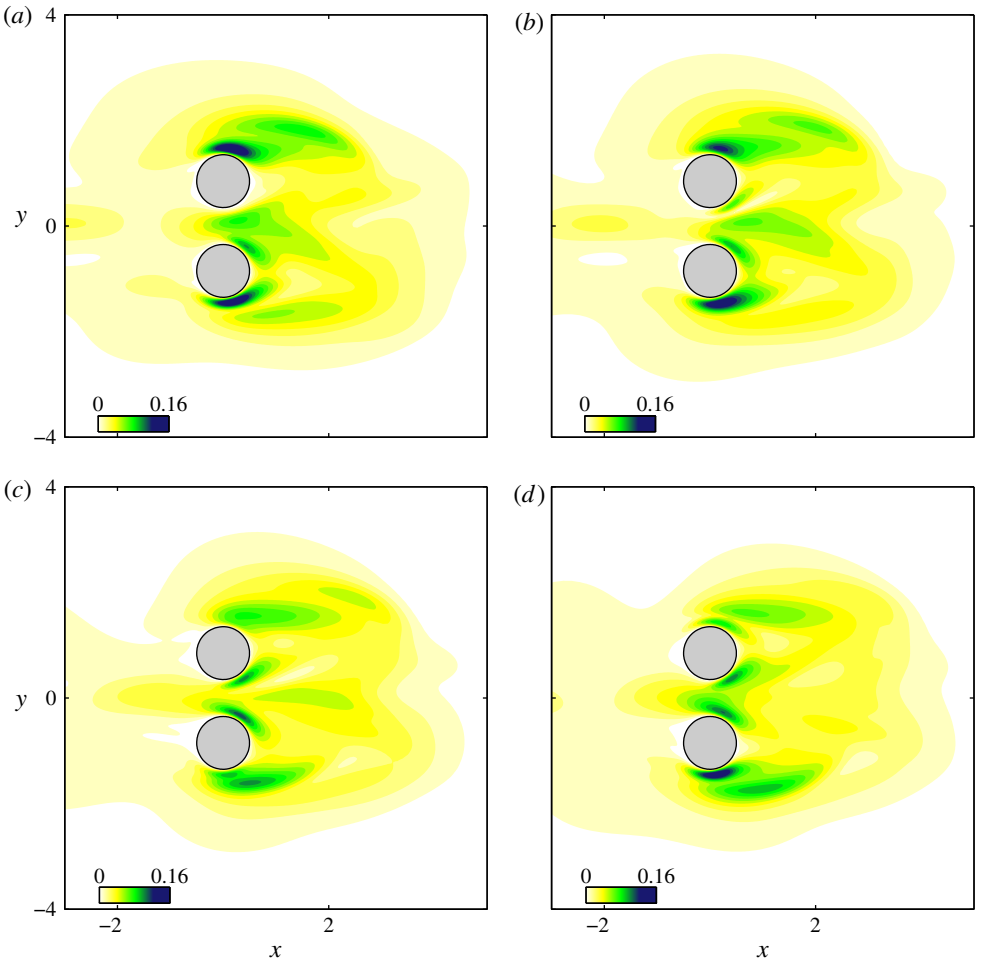

FIGURE 15. (Colour online) Spatial distribution of the adjoint Floquet mode at $g = 0.7$ and $Re = 61.8$: modulus of the velocity field $\|\hat{\boldsymbol{f}}^{+}\|$. Four subsequent shedding phases ϕ are illustrated among the eight in which the vortex shedding cycle has been equally divided: (*a*) $\phi = 0$; (*b*) $\phi = \pi/4$; (*c*) $\phi = \pi/2$; (*d*) $\phi = 3\pi/4$. The remaining phases can be recovered by symmetry.

peaks changes with time during the shedding cycle. More precisely these peaks reach their maximum intensity at the shedding phase corresponding to the detachment of the gap vortex (figure 17*a*), being located just upstream of the detachment point.

6. Conclusions

The flip–flopping behaviour of the flow past two side-by-side circular cylinders has been often interpreted as a bistable condition between dual asymmetric states. This interpretation was mainly suggested by experimental observations at high Reynolds numbers indicating that the gap flow flip-over occurs almost randomly and with a characteristic time scale several orders of magnitude greater than that of the vortex shedding (Kim & Durbin 1988). More recently, the bistability conjecture has been supported by Mizushima & Ino (2008) based on the existence of the unstable AS

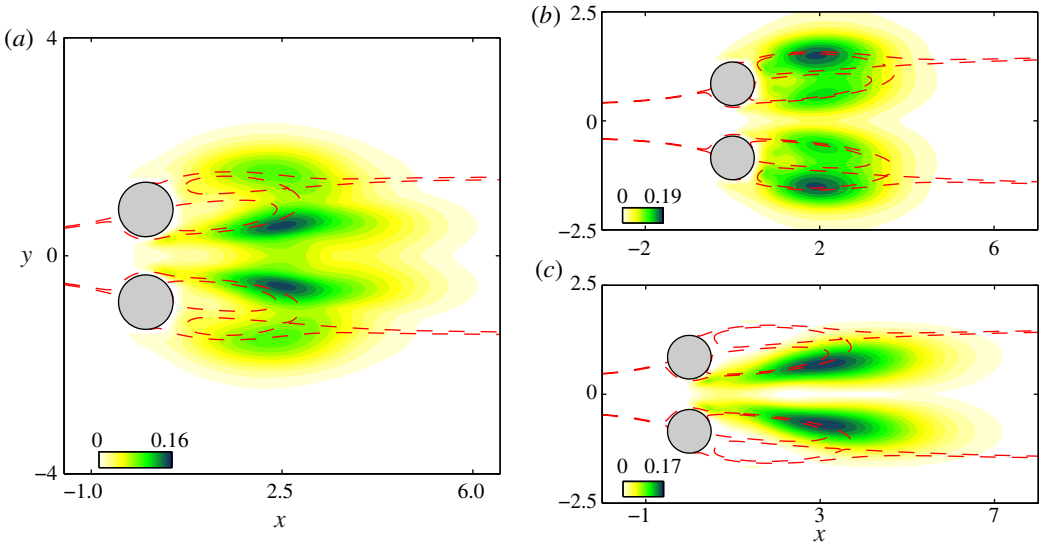

FIGURE 16. (Colour online) Structural sensitivity map: spectral norm of the sensitivity tensor field $\boldsymbol{S}(x, y)$. The results obtained for the unstable Floquet mode (see (2.8)) are illustrated for $g = 0.7$ and $Re = 61.8$ (*a*), compared with those pertaining to the unstable IP (*b*) and AS (*c*) modes on the steady symmetric base flow computed for the same values of g and Re. Dashed lines are used to illustrate regions of recirculating fluid associated with the steady base flow (*b*, *c*) and with the period average base flow (*a*).

mode on the steady symmetric base flow. In the present work, a different explanation for the origin of the flip–flop at low Reynolds numbers is proposed and motivated. The new transition scenario is based on a numerical analysis of the two-dimensional flow in the range of gap spacing $0.6 < g < 1.4$ and Reynolds numbers $50 < Re \leqslant 90$ for which the emerging of a flip–flopping pattern has been first described by Kang (2003).

The transition from the in-phase synchronized vortex shedding to the flip–flopping state has been first investigated by means of DNS for $g = 0.7$. Below the critical threshold, the resulting in-phase vortex shedding is shown to be characterized by the formation of a single large-scale vortex street developing from the outer shear layers. Meanwhile, during a shedding cycle, the smaller inner vortices are entrained and merged on opposite sides of the outer wake. With the onset of the flip–flop state the vortex dynamics is substantially modified. Both gap vortices are amalgamated on the same side of the large-scale street and the merging direction smoothly changes according to a slow harmonic oscillation which affects both the force coefficients and the gap flow. The related frequency is found to be one order of magnitude lower than that of vortex shedding and it compares well with the value reported by Kang (2003) at $Re = 100$ and $g = 1.0$.

The global stability analysis of the in-phase periodic base flow has confirmed that a pair of complex-conjugate Floquet exponents becomes unstable above the critical threshold of $g = 0.7$, $Re = 61.74$ having a frequency which is close to the low St peak extracted from DNS. Starting from this result, the stability analysis has been extended to cover an entire range of gap spacing. The resulting instability region in the parameter space, bounded by the Floquet neutral curve, ranges from $g \approx 0.6$ to $g \approx 1.4$ in the interval of Reynolds numbers $50 < Re \leqslant 74$. As compared with the bistability conjecture proposed by Mizushima & Ino (2008) based on the primary

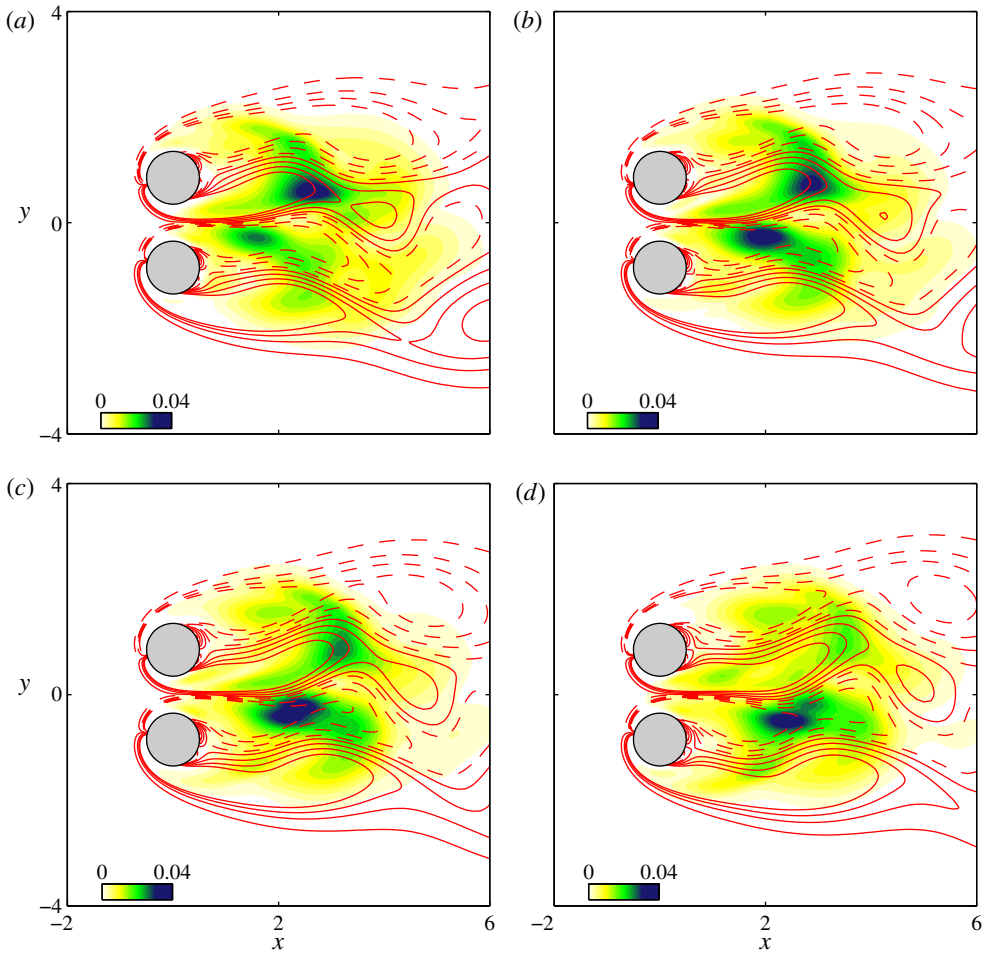

FIGURE 17. (Colour online) Results of the structural sensitivity analysis at $g = 0.7$ and $Re = 61.8$: spectral norm of tensor $\boldsymbol{I}(x, y, t)$ and vorticity of the base flow (dashed and continuous lines respectively corresponding to levels going from -1 to -0.1 and from 0.1 to 1 by steps of 0.3). Four subsequent shedding phases ϕ are illustrated among the eight in which the vortex-shedding cycle has been equally divided: (*a*) $\phi = 0$; (*b*) $\phi = \pi/4$; (*c*) $\phi = \pi/2$; (*d*) $\phi = 3\pi/4$. The remaining phases can be recovered by symmetry.

instability of the AS mode ($0.594 \leqslant g \leqslant 0.607$), this new explanation of the origin of the flip–flopping behaviour seems to be more realistic. In fact it is relevant on a wider range of gap spacing, where the flip–flop occurs ($0.2 \lesssim g \lesssim 1.2$). Moreover, the Floquet instability region agrees very well with the region where the flip–flop behaviour has been observed by Kang (2003) using DNS. Eventually, a correlation is found between the spatiotemporal pattern of the unstable Floquet mode and the nonlinear flip–flop dynamics for $g = 0.7$.

The instability core is also identified according to the structural sensitivity analysis introduced by Giannetti *et al.* (2010). The flip–flop wavemaker results mainly localized in the gap flow region and a striking similarity is found by comparing the average sensitivity map to the sensitivity map of the AS mode.

It must be noted that the relationship between the low and high *Re* flip–flop appears mainly qualitative: a clear connection between the two regimes cannot be easily established, but this point is beyond the scope of this work. Nevertheless, our analysis provides a clear evidence that the origin of the flip–flopping pattern at low *Re* has to be ascribed to the instability of the in-phase shedding cycle and not to the bistable interplay of two asymmetric states.

REFERENCES

ÅKERVIK, E., BRANDT, L., HENNINGSON, D. S., HOEPFFNER, J., MARXEN, O. & SCHLATTER, P. 2006 Steady solutions of the Navier–Stokes equations by selective frequency damping. *Phys. Fluids* **18**, 068102.

AFGAN, I., KAHIL, Y., BENHAMADOUCHE, S. & SAGAUT, P. 2011 Large eddy simulation of the flow around single and two side-by-side cylinders at subcritical Reynolds numbers. *Phys. Fluids* **23**, 075101.

AKINAGA, T. & MIZUSHIMA, J. 2005 Linear stability of flows past two circular cylinders in a side-by-side arrangement. *J. Phys. Soc. Japan* **74** (5), 1366–1369.

BEARMAN, P. W. & WADCOCK, A. J. 1973 The interaction between a pair of circular cylinders normal to a stream. *J. Fluid Mech.* **61**, 499–511.

BITTANTI, S. & COLANERI, P. 2009 *Periodic Systems: Filtering and Control (Communication and Control Engineering)*. Springer.

CAMARRI, S. & GIANNETTI, F. 2010 Effect of confinement on three-dimensional stability in the wake of a circular cylinder. *J. Fluid Mech.* **642**, 477–487.

CAMARRI, S. & IOLLO, A. 2010 Feedback control of the vortex-shedding instability based on sensitivity analysis. *Phys. Fluids* **22**, 094102.

CHEN, L., TU, J. Y. & YEOH, G. H. 2003 Numerical simulation of turbulent wake flows behind two side-by-side cylinders. *J. Fluids Struct.* **18**, 387–403.

CHOMAZ, J.-M. 2005 Global instabilities in spatially developing flows: non-normality and nonlinearity. *Annu. Rev. Fluid Mech.* **156**, 209–240.

CODDINGTON, E. & LEVINSON, N. 1955 *Theory of Ordinary Differential Equations*. McGraw-Hill.

DAVIS, T. A. 2004 Algorithm 832: UMFPACK, an unsymmetric-pattern multifrontal method. *ACM Trans. Math. Software* **30** (2), 196–199.

DRAZIN, P. G. 2002 *Introduction to Hydrodynamic Stability*. Cambridge University Press.

GIANNETTI, F., CAMARRI, S. & LUCHINI, P. 2010 Structural sensitivity of the secondary instability in the wake of a circular cylinder. *J. Fluid Mech.* **651**, 319–337.

GIANNETTI, F., FABRE, D., TCHOUFAG, J. & LUCHINI, P. 2012 The steady oblique path of buoyancy-driven rotating spheres. In *9th European Fluid Mechanics Conference, Rome, 9–13 September 2012* .

GIANNETTI, F. & LUCHINI, P. 2007 Structural sensitivity of the first instability of the cylinder wake. *J. Fluid. Mech.* **581**, 167–197.

GIANNETTI, F., LUCHINI, P. & MARINO, L. 2009 Characterization of the three-dimensional instability in a lid-driven cavity by an adjoint-based analysis. In *Seventh IUTAM Symposium on Laminar–Turbulent Transition* (ed. P. Schlatter & D. S. Henningson), pp. 96–97. KTH.

HAQUE, S., LASHGARI, I., BRANDT, L. & GIANNETTI, F. 2012 Stability of fluids with shear-dependent viscosity in the lid-driven cavity. *J. Non-Newtonian Fluid Mech.* **173**, 49–61.

ILAK, M., SCHLATTER, P., BAGHERI, S. & HENNINGSON, D. 2011 Bifurcation and stability analysis of a jet in crossflow. Part 1: Onset of global instability at a low velocity ratio. *J. Fluid Mech.* **696**, 94–121.

KANG, S. 2003 Characteristics of flow over two circular cylinders in a side-by-side arrangement at low Reynolds numbers. *Phys. Fluids* **15**, 2486–2498.

KIM, H. J. & DURBIN, P. A. 1988 Investigation of the flow between a pair of circular cylinders in the flopping regime. *J. Fluid Mech.* **196**, 431–448.

LASHGARI, I., PRALITS, J. O., GIANNETTI, F. & BRANDT, L. 2012 First instability of the flow of shear-thinning and shear-thickening fluids past a circular cylinder. *J. Fluid Mech.* **701**, 201–227.

LEHOUCQ, R. B., SORENSEN, D. C. & YANG, C. 1998 *ARPACK Users Guide*. SIAM.

LUCHINI, P. 2011 Private communication.

LUCHINI, P., GIANNETTI, F. & PRALITS, J. O. 2008 Structural sensitivity of linear and nonlinear global modes. In *Proceedings of the 5th AIAA Theoretical Fluid Mechanics Conference, 23–26 June, Seattle, Washington* pp. 1–19. Curran Associates Inc.

LUCHINI, P., PRALITS, J. O. & GIANNETTI, F. 2007 Structural sensitivity of the finite-amplitude vortex shedding behind a circular cylinder. In *Proceedings of the 2nd IUTAM Symposium on unsteady separated flows and their control, 18–22 June 2007, Corfu, Greece* (ed. M. Braza & K. Houringan), pp. 151–160. Springer.

LUST, K., ROOSE, D., SPENCE, A. & CHAMPNEYS, A. R. 1998 An adaptive Newton–Picard algorithm with subspace iteration for computing periodic solutions. *SIAM J. Sci. Comp.* **19** (4), 1118–1209.

MARINO, L. & LUCHINI, P. 2009 Adjoint analysis of the flow over a forward-facing step. *Theor. Comp. Fluid Dyn.* **23**, 37–54.

MARQUET, O., SIPP, D. & JACQUIN, L. 2008 Sensitivity analysis and passive control of cylinder flow. *J. Fluid Mech.* **615**, 221–252.

MELIGA, P., SIPP, D. & CHOMAZ, J.-M. 2010 Effect of compressibility on the global stability of axisymmetric wake flows. *J. Fluid Mech.* **660**, 499–526.

MIZUSHIMA, J. & INO, Y. 2008 Stability of flows past a pair of circular cylinders in a side-by-side arrangement. *J. Fluid Mech.* **595**, 491–507.

PESCHARD, I. & LE GAL, P. 1996 Coupled wakes of cylinders. *Phys. Rev. Lett.* **77**, 3122–3125.

PRALITS, J. O., BRANDT, L. & GIANNETTI, F. 2010 Instability and sensitivity of the flow around a rotating circular cylinder. *J. Fluid Mech.* **650**, 1–24.

RAI, M. M. & MOIN, P. 1991 Direct simulations of turbulent flow using finite-difference schemes. *J. Comp. Phys.* **96**, 15–53.

ROBICHAUX, J., BALANCHADAR, S. & VANKA, S. P. 1999 Three-dimensional Floquet instability of the wake of a square cylinder. *Phys. Fluids* **11**, 560–578.

SHROFF, G. M. & KELLER, H. B. 1993 Stabilization of unstable procedures: the recursive projection method. *SIAM J. Numer. Anal.* **30** (4), 1099–1120.

SUMNER, D. 2010 Two circular cylinders in cross-flows: a review. *J. Fluids Struct.* **26**, 849–899.

SUMNER, D., WONG, S. S. T., PRICE, S. J. & PAÏDOUSSIS, M. P. 1999 Fluid behavior of side-by-side circular cylinders in steady cross-flow. *J. Fluids Struct.* **13**, 309–338.

TROTTENBERG, U., OOSTERLEE, C. & SCHÜLLER, A. 2001 *Multigrid*. Academic Press.

VIAUD, B., SERRE, E. & CHOMAZ, J.-M. 2011 Transition to turbulence through steep global-modes cascade in an open rotating cavity. *J. Fluid Mech.* **688**, 493–506.

WANG, Z. J., ZHOU, Y. & LI, H. 2002 Flow-visualization of a two side-by-side cylinder wake. *J. Flow Visual. Image Process.* **9**, 123–138.

WILLIAMSON, C. H. K. 1985 Evolution of a single wake behind a pair of bluff bodies. *J. Fluid Mech.* **159**, 1–18.

ZDRAVKOVICH, M. M. 1977 Review of flow interference between two circular cylinders in various arrangement. *Trans. ASME I: J. Fluids Engng* **99**, 618–633.

ZHOU, Y., ZHANG, H. J. & YIU, M. W. 2002 The turbulent wake of two side-by-side circular cylinders. *J. Fluid Mech.* **458**, 303–332.